The whole-brain pattern of magnetic susceptibility perturbations in Parkinson's disease

Julio Acosta-Cabronero[1], Arturo Cardenas-Blanco[1], Matthew J Betts[1], Michaela Butryn[2], Jose P Valdes-Herrera[1], Imke Galazky[2] and Peter J Nestor[1]

[1] *German Center for Neurodegenerative Diseases (DZNE), Leipziger Strasse 44, 39120 Magdeburg, Germany*

[2] *Department of Neurology, Otto-von-Guericke University, Leipziger Strasse 44, 39120 Magdeburg, Germany*

Corresponding author: Dr Julio Acosta-Cabronero

Corresponding author's address: Deutsches Zentrum für Neurodegenerative Erkrankungen e.V. (DZNE) c/o Universitätsklinikum Magdeburg, Leipziger Strasse 44, Haus 64, 39120 Magdeburg, Germany

Corresponding author's phone and fax: Tel. +49 391 67-24534; Fax +49 391 67-24530

Corresponding author's e-mail address: jac@cantab.net

Running title: Parkinson's disease magnetostatics

ABSTRACT

Although iron-mediated oxidative stress has been proposed as a potential pathomechanism in Parkinson's disease, the global distribution of iron accumulation in Parkinson's disease has not yet been elucidated. This study used a new magnetic resonance imaging contrast, quantitative susceptibility mapping, and *state-of-the-art* methods to map for the first time the whole-brain landscape of magnetostatic alterations as a surrogate for iron level changes in N=25 idiopathic Parkinson's disease patients versus N=50 matched controls. In addition to whole-brain analysis, a regional study including sub-segmentation of the substantia nigra into dorsal and ventral regions and qualitative assessment of susceptibility maps in single subjects were also performed. The most remarkable basal ganglia effect was an apparent magnetic susceptibility increase—consistent with iron deposition—in the dorsal substantia nigra, though an effect was also observed in ventral regions. Increased bulk susceptibility, additionally, was detected in rostral pontine areas and in a cortical pattern tightly concordant with known Parkinson's disease distributions of α-synuclein pathology. In contrast, the normally iron rich cerebellar dentate nucleus returned a susceptibility reduction suggesting decreased iron content. These results are in agreement with previous post-mortem studies in which iron content was evaluated in specific regions of interest; however, extensive neocortical and cerebellar changes constitute a far more complex pattern of iron dysregulation than was anticipated. Such finding also stand in stark contrast to the lack of statistically significant group change using conventional magnetic resonance imaging methods namely voxel-based morphometry, cortical thickness analysis, subcortical volumetry and tract-based diffusion tensor analysis; confirming the potential of whole-brain quantitative susceptibility mapping as an *in vivo* biomarker in Parkinson's disease.

INTRODUCTION

Idiopathic Parkinson's disease is a common progressive degenerative disorder characterised pathologically by proteinaceous aggregates of α-synuclein in the form of Lewy bodies and Lewy neurites. These are thought to occur early in the brainstem, gradually spreading across vulnerable sites in the allocortex and temporal paralimbic cortex before reaching prefrontal and sensory-association isocortex (Braak *et al.*, 2004). It is postulated that projection neurons with disproportionally long, thin and poorly myelinated axons are particularly susceptible to degeneration in Parkinson's disease (Braak *et al.*, 2004), of which the most studied to date have been the neuromelanin-pigmented dopaminergic neurons of the basal ganglia. It should be noted, however, that the mechanisms that render certain neuronal populations vulnerable to degeneration are unclear; furthermore, the motor dysfunction in Parkinson's disease related to nigrostriatal degeneration is only one aspect of this multi-faceted disease that includes numerous non-motor

manifestations. As such, new *in vivo* approaches to identify possible pathomechanisms across the entire Parkinson's disease brain are highly desirable.

One such potential mechanism is oxidative stress due to excessive brain iron accumulation. In the aging brain, this has been implicated in neurotoxicity, mitochondrial dysfunction and chronic inflammation, as well as promotion of α-synuclein aggregation and dopaminergic alterations (Sian-Huelsmann *et al.*, 2011; Ayton and Lei, 2014). The relevance of iron in the pathogenesis of Parkinson's disease lies in its capacity to generate free-radical species that may act in concert with α-synuclein to induce Lewy pathology (Ostrerova-Golts *et al.*, 2000; Li *et al.*, 2011), and may catalyse dopamine oxidation reactions that exacerbate the formation of other neurotoxic by-products (Hare and Double, In Press, DOI: 10.1093/brain/aww022, available online 8 March 2016). The study of brain iron, however, is particularly challenging due to its ubiquitous involvement in numerous biological processes (Ward *et al.*, 2014). Under normal conditions, it is well established that a high proportion of brain iron is bound to ferritin in the redox-inactive ferric state (Hallgren and Sourander, 1958), whereas only small quantities of redox-active ferrous iron are required to ensure a readily available supply of labile iron for cellular metabolism. It is thus largely assumed that all mechanisms involving iron management, i.e. transport, uptake, storage, efflux and redistribution, must be stringently regulated to prevent free ferrous iron from indiscriminately catalysing additional unwanted toxic reactions. To date, however, we lack conclusive evidence incriminating free-iron mediated mechanisms as a primary cause rather than a secondary consequence of neurodegeneration in Parkinson's disease. Nonetheless, numerous studies have confirmed iron elevation in the substantia nigra pars compacta of post-mortem brains using histochemical (Dexter *et al.*, 1991; Sofic *et al.*, 1991) and X-ray methods (Popescu *et al.*, 2009), and *in vivo*, employing semi-quantitative iron-sensitive techniques such as transcranial sonography and magnetic resonance imaging (MRI) – reviewed elsewhere (Groeger and Berg, 2012); an increase that might lead to iron-mediated toxic interactions in Parkinson's disease. Thus far, however, iron analyses have been limited to regions of interest, and though several brain areas beyond the substantia nigra have been identified as having increased (Griffiths *et al.*, 1999) or decreased (Dexter *et al.*, 1991; Popescu *et al.*, 2009) iron content, the global distribution of iron dysregulation in Parkinson's disease has not yet been elucidated. The present study utilised quantitative susceptibility mapping or QSM—a newly validated, iron-sensitive MRI measure (Langkammer *et al.*, 2012; Zheng *et al.*, 2013; Sun *et al.*, 2015)—to describe the whole-brain distribution of magnetostatic alterations in Parkinson's disease, and contrasted these results with those from "standard" structural and microstructural MRI markers, none of which, however, probes the integrity of the substantia nigra.

MATERIALS AND METHODS

Study subjects

N=25 clinically definite idiopathic Parkinson's disease patients according to UK Parkinson's Disease Brain Bank criteria (Hughes *et al.*, 1992) were recruited from the specialist movement disorder clinic of the Otto von Guericke University Neurology Department. All patients had their clinical assessments in the 'on' state with respect to anti-Parkinsonian medication with the exception of one mild, drug-naïve, tremor-dominant individual who wished to delay commencing therapy until symptoms worsened. For imaging comparisons, N=50 healthy control subjects—a subset of a larger, previously studied, aging cohort (Acosta-Cabronero *et al.*, 2016)—were twice-paired for age while keeping a non-significant sex ratio. All controls performed normally on cognitive screening, mini-mental state examination or MMSE (Folstein *et al.*, 1975), and had no history of neurological disease. Group demographic details are summarised in Table 1.

Table 1. Study demographic details.

	Control (N=50)	**Parkinson's disease (N=25)**
Sex (male:female)	28:22	20:5 [χ^2=9.7, NS]
Age (years)	63.6 (8.5)	63.6 (8.6)
Disease duration (years)	NA	6 (4)
MMSE (≤30)	29.0 (0.9)	26.7 (3.0)
UPDRS-III (≥0)	NA	16.3 (8.0)
Tremor dominant/akinetic-rigid dominant/mixed (N, %)	NA	12/52/36
Modified Hoehn & Yahr stage (≥1)	NA	2.2 (0.3)
Levodopa equivalent dose (mg)	NA	748 (434)

Where appropriate values are given as mean (standard deviation); not significant (NS, P>0.01); not applicable (NA); mini-mental state examination (MMSE); on-medication, unified Parkinson's disease rating scale – motor evaluation (UPDRS-III).

Prior to inclusion in the study, which was approved by the ethics committee at Otto-von-Guericke University, subjects gave their written informed consent according to the Declaration of Helsinki.

Imaging protocol

The imaging protocol and processing methods used in this study are identical, except for the addition of diffusion tensor imaging (DTI), to those developed and optimised for a previous aging study (Acosta-Cabronero *et al.*, 2016), which are summarised below:

MRI measurements were performed on a Siemens Verio 3 Tesla system (Siemens, Erlangen, Germany) with a standard Siemens 32-channel receive array coil.

Susceptibility weighting was sensitised with a three dimensional, flow-compensated, spoiled gradient-echo pulse sequence: flip angle was 17°; echo time, 20 ms; receiver bandwidth, 100 Hz per pixel; and repetition time, 28 ms. Matrix size was 256×224×80, with slices in straight-axial orientation (0.4-mm inter-spacing and 20% oversampling to reduce crosstalk effects and aliasing artifacts, respectively), and voxel resolution of $1\times1\times2$ mm^3. GRAPPA, the technique of generalised autocalibrating partially parallel acquisitions (Griswold *et al.*, 2002), was used with acceleration factor of 2 and 24 reference lines, giving a scan time of 5:32 minutes.

MPRAGE (magnetisation-prepared, three dimensional, rapid gradient-echo) anatomical images were also acquired with the following acquisition parameters: inversion time was 1100 ms; flip angle, 7°; echo time, 4.37 ms; receiver bandwidth, 140 Hz/pixel; echo spacing, 11.1 ms; and repetition time, 2500 ms. Matrix dimensions were 256×256×192 (0.5-mm inter-slice gap), 7/8 partial Fourier, and $1\times1\times1$ mm^3 voxel size. GRAPPA was also enabled with acceleration factor of 2 and 24 reference lines. To aid co-registration, the field of view was prescribed consistent with the susceptibility-weighted scan, i.e. with slices in straight-sagittal orientation.

T_2-weighted turbo spin echo images were also acquired in the same scanning session, and were visually inspected to ensure vascular pathology—as for standard clinical practice—was not significant in any subject. To facilitate visual inspection, the field of view was aligned at acquisition to the anterior commissure–posterior commissure line. Scan parameters were: flip angle, 150°; echo time, 96 ms; receiver bandwidth, 220 Hz/pixel; turbo factor, 18; 13 echo trains with echo spacing, 9.64 ms; and repetition time, 8160 ms. In-plane matrix was 320×320 (resolution: 0.7×0.7 mm^2) for 45 axial slices (thickness: 3 mm; gap: 0.9 mm); GRAPPA factor of 2 with 51 reference lines.

Diffusion MRI data was acquired using a twice-refocused, single-shot echo-planar imaging pulse sequence: repetition/ echo time = 9000/ 94 ms; matrix, 120×120; 63 contiguous slices aligned parallel to the anterior commissure–posterior commissure line; voxel size: $2\times2\times2$ mm^3; 7/8-phase partial Fourier; bandwidth of 1667 Hz/pixel and echo spacing of 0.68 ms. Diffusion gradients were applied along 30 non-collinear directions with two non-zero b-values (b=700 and 1000 s/mm^2), and 12 interleaved reference scans. Parallel imaging was enabled (GRAPPA, acceleration factor of 2 and 38 reference lines) for a total scan time of 11:15 minutes.

A thin pillow was placed on the base of the coil surrounding the sides and the back of the head to minimise motion and increase inter-subject reproducibility in positioning.

Structural MRI statistical analyses

Voxel-based morphometry. VBM was performed in SPM12b v6080 (http://www.fil.ion.ucl.ac.uk/spm/software/spm12) with default settings. Following "unified segmentation" and "modulation", grey matter segments were smoothed with an 8-mm full width at half maximum Gaussian kernel prior to statistical analysis – a two sample (Parkinson's disease versus control) T-test controlling for total intracranial volume; the latter were determined using a previously validated method (Pengas *et al*., 2009).

Cortical thickness analysis. A standard whole-brain routine for vertex-wise surface reconstruction, inflation, smoothing and statistical group analysis of cortical thickness was carried out in the FreeSurfer v5.3.0 framework (http://surfer.nmr.mgh.harvard.edu).

Subcortical volumetry. Left and right thalamus, caudate nucleus, putamen, globus pallidus, hippocampus and amygdala were segmented automatically from radio-frequency bias-corrected MPRAGE images using the FIRST algorithm (Patenaude *et al.*, 2011) – an automated surface-aware method that incorporates prior anatomical knowledge (included in FMRIB's software library, FSL v5.0.9). FIRST-derived region of interest volumes were normalised by total intracranial volume using a well-established covariance method (Jack *et al.*, 1989). Finally, n=12 two-tailed Wilcoxon rank-sum tests of equal medians were performed to assess for group differences in each region of interest.

DTI analysis. Diffusion MRI datasets were processed with a standard procedure in FSL v5.0.9 (http://fsl.fmrib.ox.ac.uk/fsl/fslwiki/FDT). DTI metrics (fractional anisotropy, FA, and mean diffusivity, MD, calculated from weighted least-squares tensor fits) were introduced into the tract-based spatial statistics (Smith *et al.*, 2006) v1.2 routine with default settings, which generated a mean FA skeleton (default FA threshold set to 0.2) to assess white matter tracts, i.e. it did not include the substantia nigra or other grey matter regions. Finally, whole-brain group contrasts (Parkinson's disease versus controls) for FA and MD were inferred using Randomise v2.9 (Winkler *et al.*, 2014) in FSL with 5,000 permutations of the data and default settings for threshold-free cluster enhancement (Smith and Nichols, 2009), i.e. two-dimensional optimisation for tract-based DTI analysis.

QSM reconstruction

Multi-channel complex data were combined using a modified adaptive algorithm (Walsh *et al.*, 2000). Combined phase images were then unwrapped with a continuous Laplacian approach (Schofield and Zhu, 2003), and the local field was revealed through global extraction of the background field using the spherical mean value filtering method (Schweser *et al.*, 2011) with sphere radius of 5 mm. Finally, susceptibility maps were estimated with the morphology-enabled, non-linear dipole inversion formulation (Liu *et al.*, 2013) solved by the conjugate gradient method on iterative blocks of 500 operations nested in a Gauss-Newton loop with stopping tolerance ratio for the outer loop set to 0.01. For consistency with our previous aging study (Acosta-Cabronero *et al.*, 2016) using the exact same MRI scan and QSM routine, the Lagrangian multiplier was set to λ=1000. Our previous study also suggested reference normalisation is only a small adjustment relative to aging effects. In this study, thus, to avoid making assumptions about areas being spared in Parkinson's disease, QSM values were not referenced.

QSM spatial standardisation

For template creation, radio-frequency bias corrected MPRAGE images were spatially normalised using the 'Greedy-SyN' approach in ANTs v2.1 (http://stnava.github.io/ANTs) with a maximum of 90×30×30 multi-resolution iterations and template-update step size set to 0.1 mm. Rigid-plus-affine initial alignment was followed by six full runs of the above routine. Subsequently, bias-corrected magnitude images were affine co-registered to their corresponding MPRAGE volume. QSM spatial standardisation was achieved through the warp composition of the above transformations and third-order b-spline interpolation. An average template was then calculated across all warped QSMs.

Whole-brain QSM statistical analyses

Analyses were performed both for signed and absolute QSM. The absolute value was taken to QSM to improve statistical conditioning for whole-brain analysis (Betts *et al.*, 2016) and to ameliorate the spurious impact of blooming effects, i.e. residuals in the vicinity of steep magnetic susceptibility gradients. Smoothing is a requirement in this context to correct for co-registration errors and other imperfections, thus a 3D-Gaussian kernel (standard deviation: 3 mm) was applied followed by a previously proposed smoothing-compensation strategy (Betts *et al.*, 2016). Whole-brain (Parkinson's disease versus control) permutation analysis was performed with Randomise v2.9 and threshold-free cluster enhancement (with '-T' settings, http://fsl.fmrib.ox.ac.uk/fsl/fslwiki/Randomise) in FSL. Significant clusters were inferred from 20,000 data permutations and were reported at a family-wise error (FWE) corrected threshold level of 0.05. The group comparison was performed in two stages: first, we tested the null-hypotheses

that age and sex did not co-vary with group behaviours, which returned a widespread distribution of strong positive age effects, whereas the same null hypothesis for sex could not be rejected. The second (reporting) stage, therefore, tested whether age-adjusted QSM group medians were equal. Finally, to assess whether QSM might predict disease severity, permutation-based whole-brain QSM regression analyses versus severity scores, i.e. UPDRS-III and MMSE, were also performed.

Subsequently after analysis, the QSM template and statistical maps were warped into MNI152 space (Montreal Neurological Institute, McGill University, Canada) using ANTs tools. Affected brainstem structures were discerned using Duvernoy's atlas – the upper pons was identified axially on the standardised QSM template across z=-28 mm (in MNI coordinates); high pons at the level of the nucleus coeruleus, across z=-25 mm; high pons at the level of the lateral lemniscus, across z=-22 mm; mesencephalon at the level of the inferior colliculus, across z=-19 mm; mesencephalon at the level of the inferior pole of the red nucleus, across z=-13 mm; and mesencephalon at the level of the red nucleus, across z=-10 mm.

Regional QSM statistical analysis

The primary objective of the present study was to map the whole-brain landscape of QSM alterations in Parkinson's disease; post-hoc regional analyses in this context, therefore, aimed at providing additional insight into the nature of such alterations. Median QSM values were extracted bilaterally from the following structures: caudate nucleus, putamen, globus pallidus, hippocampus, amygdala and thalamus – inferred automatically from the study-wise MPRAGE template using FSL-FIRST. In addition, QSM data was also extracted from previously validated manual segmentations of the red nucleus, substantia nigra and dentate nucleus (Acosta-Cabronero *et al.*, 2016). Further segmentation of the substantia nigra is particularly complex because its two main substructures—dorsally, pars compacta and ventrally, pars reticulata—overlap (Lehericy *et al.*, 2014). Neuromelanin-rich dopaminergic neurons of the dorsal substantia nigra, however, possess differential spin-lattice relaxation properties resulting in T_1 shortening effects. Such effects are typically too subtle for reliable identification in single subjects but they can be resolved on *state-of-the-art* T_1-weighted templates. Fig. 1 illustrates the nigral subdivision into dorsal (hyperintense) and ventral (hypointense) tiers. Both subregions were traced three-dimensionally using FSL's image viewer (FSLView). Finally, all subcortical regions of interest were eroded by convolution with a 1-mm radius spherical kernel and were visually inspected on each template-warped QSM to ensure partial-volume contamination due to warping errors was not significant.

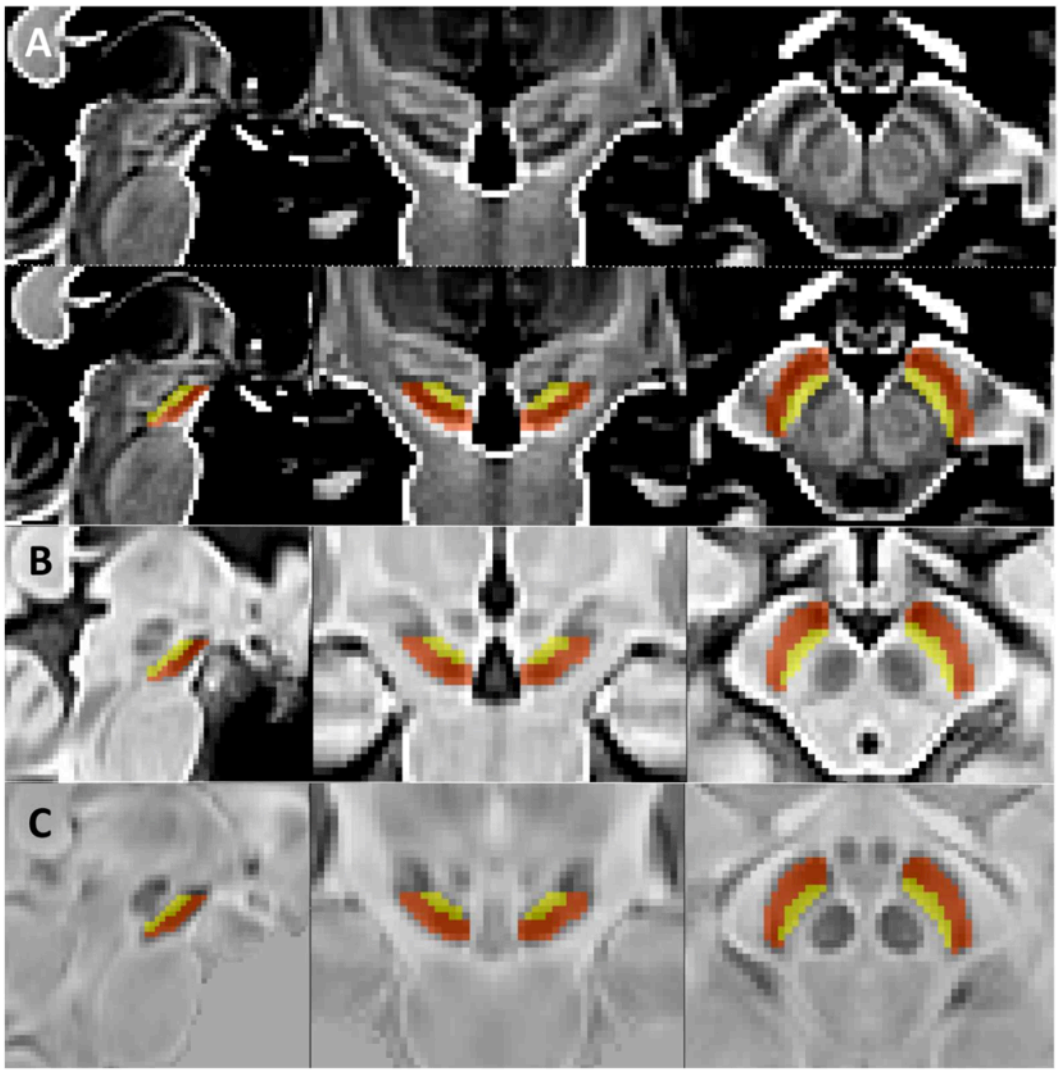

Figure 1. Manual substantia nigra subdivision. Representative sagittal, coronal and axial views of the midbrain region for the (A, top) T_1-weighted average template, and for nigral subregions overlaid onto (A, bottom) T_1-weighted, (B) T_2*-weighted and (C) QSM templates. Dorsal and ventral tiers are denoted by yellow and orange overlays, respectively.

In light of the whole-brain results, a set of cortical regions of interest were also examined; these were defined from the gyral-based Desikan-Killiany-Tourville digital atlas (Klein and Tourville, 2012) overlaid onto the statistical map of QSM group differences. The OASIS-30 template and OASIS-TRT-20 joint fusion atlas (in OASIS-30 space) were obtained from Mindboggle's repository (http://www.mindboggle.info/data). The study-wise to OASIS-30 space nonlinear warp field was calculated with a deformable b-spline co-registration routine in ANTs ('antsRegistrationSyN'). Desikan-Killiany-Tourville labels were brought into the study space using the inverse of such transformation and nearest-neighbour interpolation. Finally, to minimise partial-volume contamination, each cortical region of interest was intersected with a study-wise grey matter mask – the control-average grey matter segment binarised at a grey matter density cut-off of

0.5. Grey matter probability segments were inferred from anatomical MPRAGE images using SPM12 with default "unified segmentation" settings, and were then spatially normalised using ANTs template transforms. The pattern of QSM involvement in the Parkinson's disease cortex led to the selection of six regions of interest – four putative and two control regions. The former were lateral occipital, middle temporal, posterior parietal (including inferior and superior parietal lobules plus precuneus regions), and rostral middle prefrontal cortex. Pre- and postcentral gyri were selected as control regions.

Inter-hemispheric differences were probed using Wilcoxon rank-sum tests, which revealed that left/right measurements were comparable across patients and controls both in the cortex and in deep grey matter structures (all $P>0.15$). Thus, to improve measurement stability, median region of interest values were averaged across hemispheres and Pearson age-correlation tests were performed; these, together with the age effects observed in stage 1 of the whole-brain analysis, confirmed that the present age range is sufficiently large to modulate QSM behaviours. Consequently, prior to computing Parkinson's disease-versus-control Wilcoxon rank-sum statistics, QSM values were age-corrected using the covariance method (Jack *et al.*, 1989). Finally, Pearson correlation tests were performed to test the null-hypotheses: QSM in patients does not co-vary with UPDRS-III or MMSE. All regional tests were performed two-tailed, and their resulting P-values were Bonferroni-adjusted to minimise multiple testing effects.

Computing platform

Except where stated otherwise, processing tasks (including QSM reconstruction and regional data analysis) were prototyped and executed in the MATLAB R2012a environment (The Mathworks Inc., Natick, MA, USA).

RESULTS

Structural analyses

The structural measures—subcortical volumetry, voxel-based morphometry, cortical thickness analysis and tract-based DTI statistics—were all negative in the Parkinson's disease versus age-matched control group comparison, i.e. they failed to reject the null-hypothesis of equal means or medians at an uncorrected statistical threshold of $P<0.01$.

Whole-brain QSM study

In contrast, the whole-brain QSM group results (Fig. 2 and Fig. 3) revealed widespread absolute susceptibility increases (family-wise error corrected $P<0.05$) in Parkinson's disease that involved

brainstem, cerebral and cerebellar structures. Largely bilateral abnormalities were identified in the rostral pons (z=-34 to -25, y=-25 and x=-8 to 15 mm, including the site of the basal pontis and superior areas of the pontine tegmentum); in the superior cerebellar peduncle; caudal mesencephalon (z=-22 to -13, y=-16, x=-8 to 8 mm, including dorsal substantia nigra and inferior midbrain tegmental areas); temporal lobe structures (z=-43 to 11, y=-58 to -16, x=-44 and 44 mm, including portions of superior, middle and inferior temporal, fusiform, parahippocampal, entorhinal regions and the hippocampal head, with a marked right bias and largest cluster centred around the intermediate part of the right temporal lobe, z=-19 to -13 mm, y=-25 to -16, x=44 mm); occipital regions (z=-13 to -53, y=-87 to -58, x=-44 to 44 mm, most intense in left lateral areas but also involving lingual, pericalcarine and cuneus cortices); posterior parietal regions (z=17 to 68, y=-70 to -58, x=-15 to 15 mm, also left lateralised including large sections of the inferior and superior parietal lobules, precuneus and isthmus of the cingulate cortex); and prefrontal areas (z=-25 to 50, y=24 to 50, x=-44 to 44 mm, most markedly across the rostral middle prefrontal cortex but also touching on orbitofrontal areas and the pars triangularis of the inferior frontal lobe). Although more patchy, some regions in the insula and cerebellar cortex were also involved. In contrast, QSM in primary sensory-motor fields of the precentral and postcentral gyri, most of the remaining insula, extra-nigral nodes of the basal ganglia and diencephalic structures did not return statistical differences between groups. The opposite behaviour (i.e. reduced absolute susceptibility in Parkinson's disease) was not statistically significant at a whole brain-corrected level. Significant clusters for increased signed QSM—albeit less extensive—were highly co-localised with those for absolute QSM (not shown).

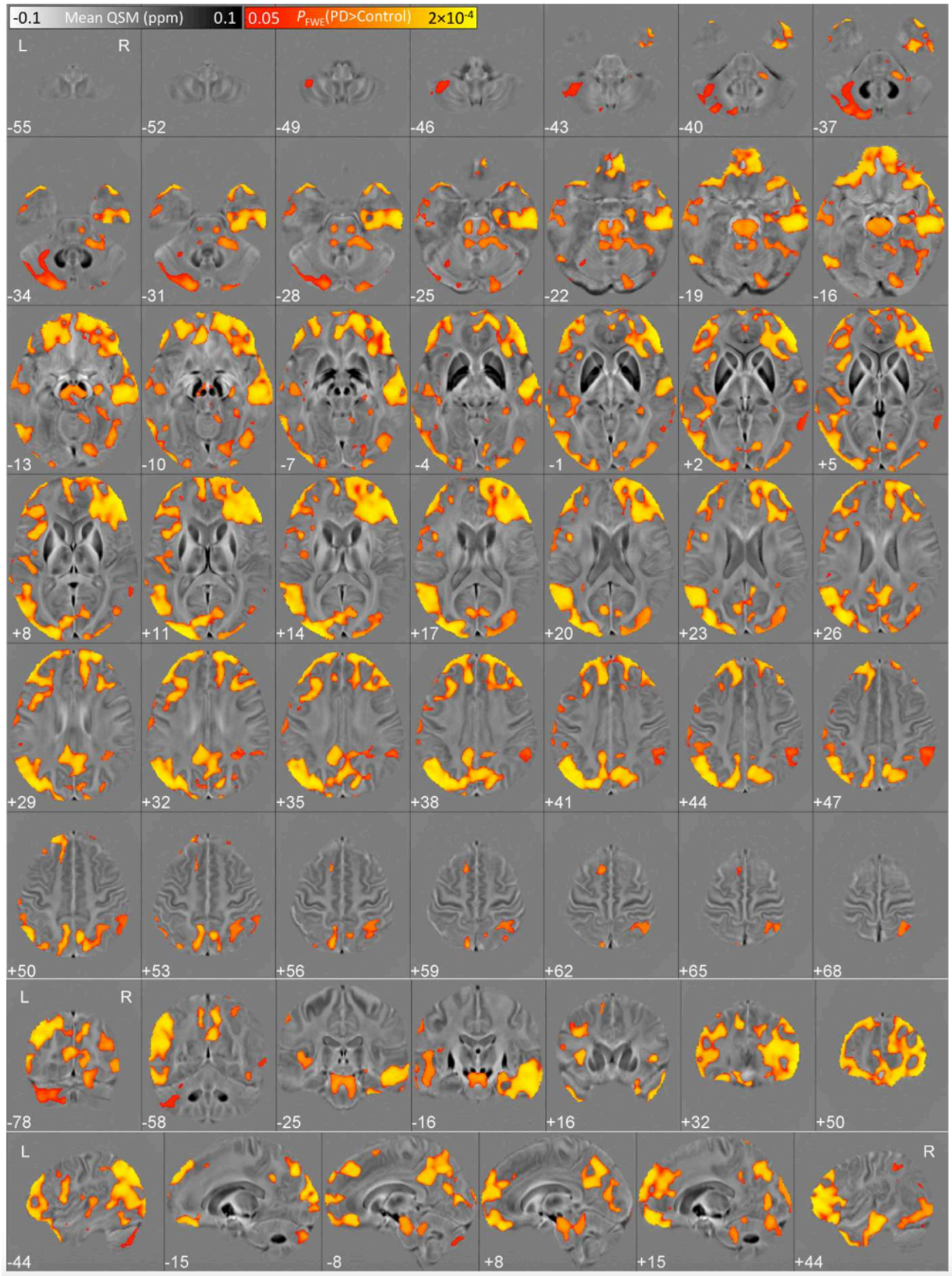

Figure 2. Cluster-based QSM group statistics (N=25 Parkinson's disease patients vs. N=50 elderly controls) for the contrast: age-corrected QSM greater in Parkinson's disease than in controls.

Results were overlaid onto the study-wise QSM template in the MNI coordinate system. Red/yellow clusters represent statistical differences at $P_{FWE}<0.05$.

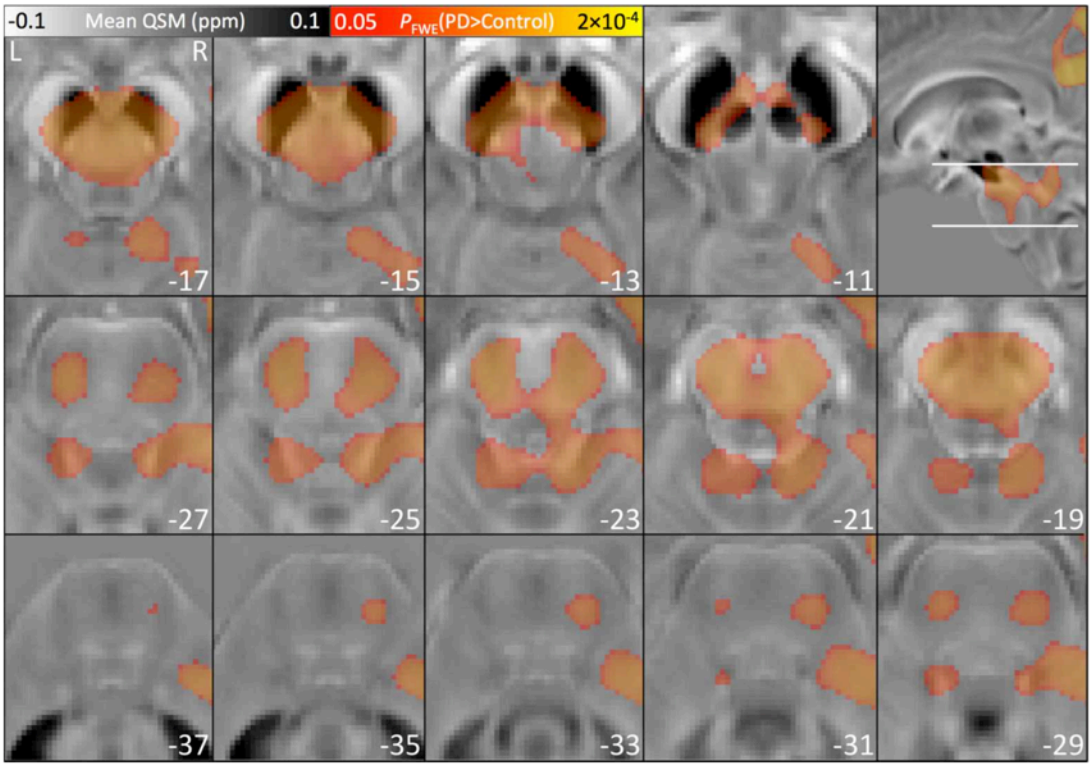

Figure 3. QSM group results with focus on rostral pons and caudal mesencephalic areas. Results were overlaid onto the QSM template in MNI space. Semi-transparent blobs represent statistical differences at $P_{FWE}<0.05$.

QSM regression analyses versus symptom severity measures, UPDRS-III or MMSE, did not return any significant correlation cluster at the whole-brain level ($P_{FWE}<0.05$).

Single-subject QSM examination

Closer inspection of midbrain and cerebellar nuclei demonstrated QSM abnormalities that were apparent on visual inspection of individuals (Fig. 4). The most striking effect—consistent with the whole-brain results—was observed in the dorsal substantia nigra region. Particularly remarkable was the disappearance in most Parkinson's disease cases of two lateral hyperintense pockets that can be readily identified in the caudal region of most healthy subjects (Fig. 3). Increased susceptibility, however, was also noticeable in the ventral substantia nigra – chiefly in rostral areas. The cerebellar dentate nucleus (Fig. 4) was also abnormal in Parkinson's disease but in the opposite direction with several subjects presenting very little or no contrast on QSM.

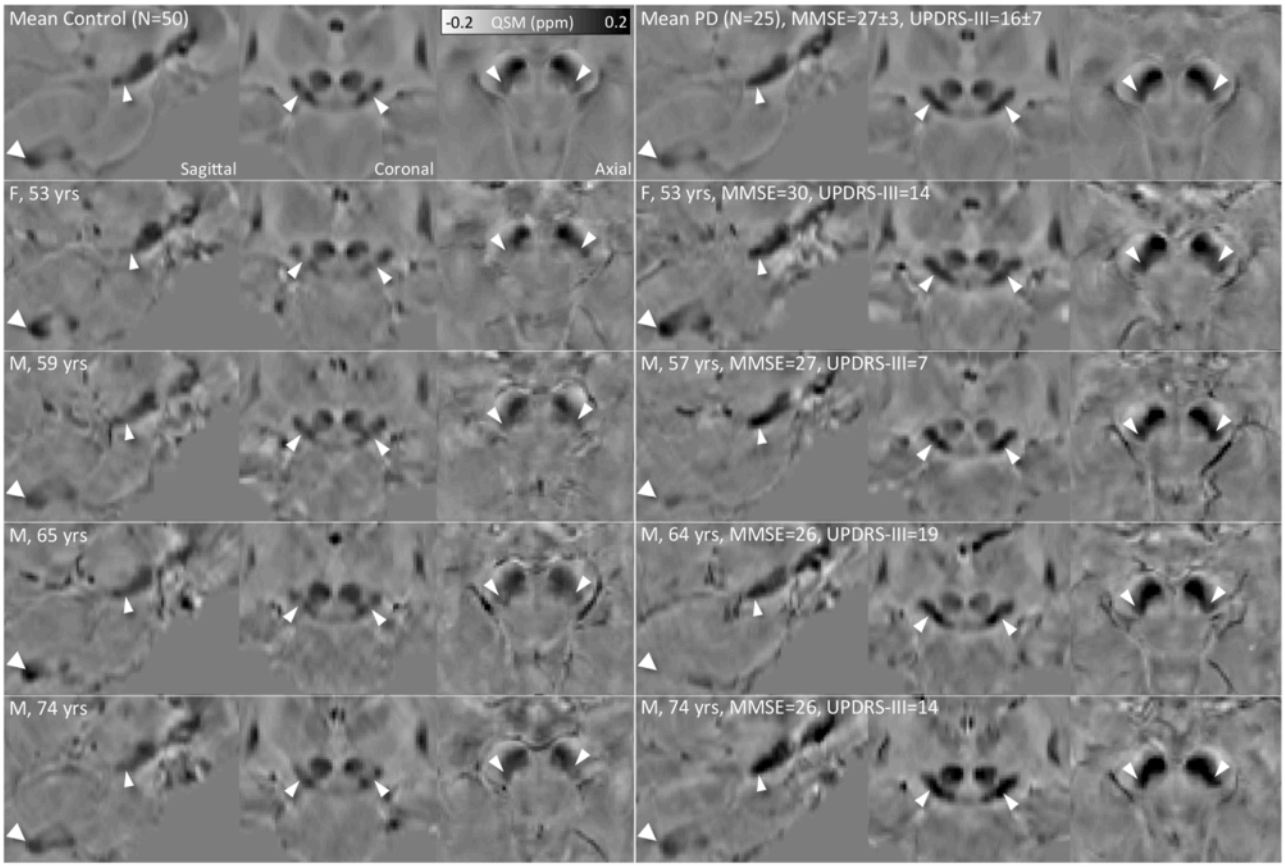

Figure 4. Magnified views of brainstem and cerebellar nuclei for QSM group-average and individual Parkinson's disease/paired-control subjects. Arrowheads denote nigrosome-1 in dorsal substantia nigra (thinner arrows, increased QSM in Parkinson's disease) and dentate nucleus (thicker arrows, decreased QSM in Parkinson's disease).

Regional QSM study

In the control group, strong QSM-age dependencies (i.e. statistically significant Pearson correlations) were identified in several subcortical and cortical regions of interest including putamen, middle temporal and prefrontal structures (Fig. 5). Group statistics were thus calculated with age-corrected absolute QSM data (Fig. 6), which returned strong alterations in the substantia nigra —mostly driven by increased susceptibility in the dorsal tier though also apparent in ventral regions—, lateral occipital, posterior parietal and rostral middle prefrontal cortical regions with additional—though less pronounced—increases in the middle temporal gyrus and hippocampus. The cerebellar dentate nucleus region of interest again showed the opposite pattern with significantly decreased susceptibility. Although effect sizes were overall smaller, regional behaviours for signed QSM (not shown) were highly concordant with those reported in Fig. 5 and 6 for absolute QSM.

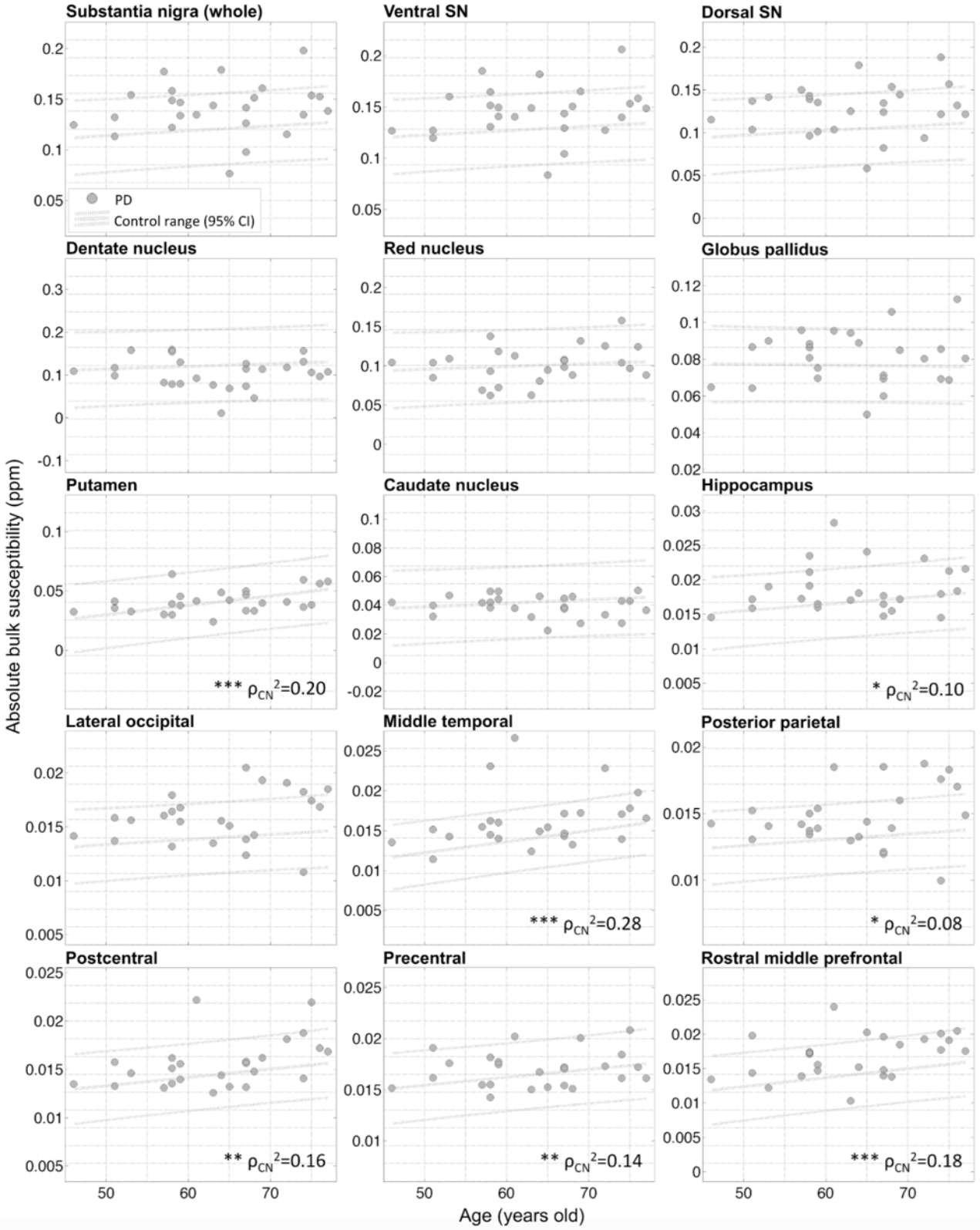

Figure 5. Regional QSM as a function of age. Median QSM values in Parkinson's disease plotted in relation to their matched-control range. Stars signify the strength of the age-correlation in the control group (*** $P_{Bonferroni}<0.05$; ** $P<0.01$; * $P<0.05$). To aid comparability, *y*-axes were clipped at six standard deviations around the global control mean.

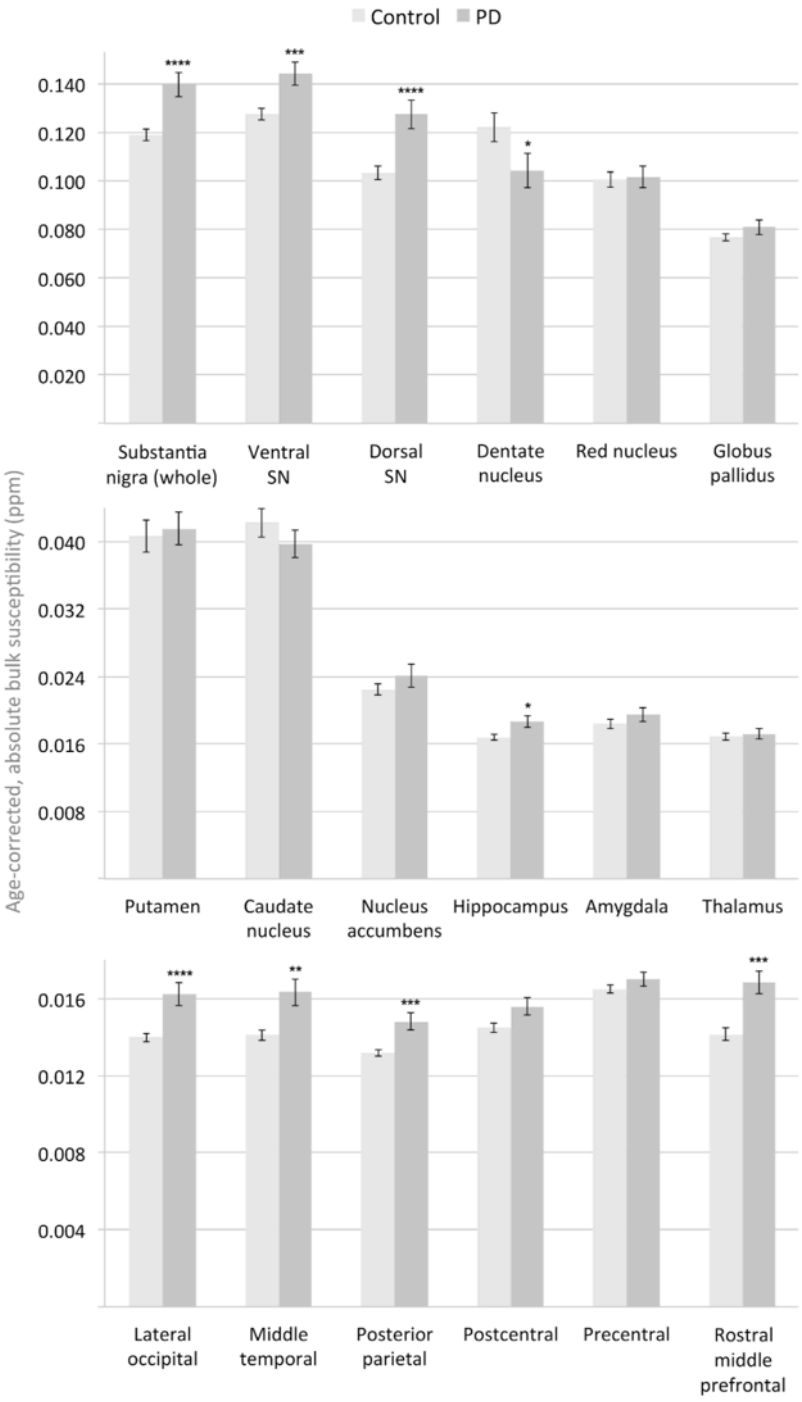

Figure 6. Summary of age-corrected QSM statistics (mean±S.E.M). Stars signify the strength of the group difference (**** $P_{Bonferroni}<0.01$; *** $P_{Bonferroni}<0.05$; ** $P<0.01$; * $P<0.05$).

In general, consistent with the whole-brain analyses, regional QSM values did not correlate with UPDRS-III or MMSE (Supplementary Fig. 1 and Supplementary Fig. 2, respectively), although there was a possible suggestion of motor-score correlation in post- ($\rho^2=0.27$, $P<0.01$) and precentral gyri ($\rho^2=0.29$, $P<0.01$) but these did not remain significant after Bonferroni adjustment.

DISCUSSION

Using a whole-brain approach for the first time to map the landscape of magnetostatic alterations in Parkinson's disease, widespread QSM changes across the brainstem and cortex were revealed (Fig. 2). In the brainstem, abnormalities were identified in the rostral pons, including pyramidal tracts and pontine tegmental areas co-localised with the site of the locus coeruleus; the superior cerebellar peduncle; and caudal mesencephalon—seemingly spreading across pars compacta/ventral tegmental substantia nigra subregions and midbrain tegmental areas, possibly also including dorsal raphe and oculomotor nuclei (Fig. 3). Parts of the temporal paralimbic, prefrontal and occipito-parietal cortex and, less markedly, insular and cerebellar areas were also involved (Fig. 2). The striatum as well as primary motor and somatosensory fields, in contrast, were relatively spared.

Substantia nigra

Superior pontine and caudal mesencephalic Parkinson's disease involvement (Fig. 3) was an expected result in light of the many past studies that reported extensive Lewy body pathology and loss of pigmented neurons in brainstem nuclei such as locus coeruleus and substantia nigra pars compacta (Hirsch *et al.*, 1988; Braak *et al.*, 2004). Past reports have shown that iron overload in Parkinson's disease substantia nigra can be readily identified by the absence of a bilateral pocket of low paramagnetism located in the dorsolateral region – a caudal substantia nigra subregion commonly designated as substantia nigra nigrosome-1 – detectable both with 3T (Schwarz *et al.*, 2014) and 7T MRI (Kwon *et al.*, 2012; Blazejewska *et al.*, 2013; Lehericy *et al.*, 2014). The nigrosome-1 is a large cluster of melanin-rich dopaminergic neurons that do not require as much iron for their normal activity as their adjacent neighbours (Lehericy *et al.*, 2014). In Parkinson's disease, however, nigrosome-1 dopaminergic neurons progressively scavenge excess iron (Good *et al.*, 1992; Oakley *et al.*, 2007) and degenerate (Fearnley and Lees, 1991; Damier *et al.*, 1999); observations consistent with the present study in which nigrosome-1 of Parkinson's disease patients appeared overloaded with iron, which might be more readily detectable on coronal views (Fig. 4). To our knowledge—although this was not our primary objective, hence image resolution was suboptimal for this purpose—this is the first report of nigrosome-1 visualisation with QSM. In future, quantitative susceptibility evaluations of nigrosome-1 load in Parkinsonism with higher resolution MRI prescriptions optimised for midbrain imaging are warranted. On a different note, it is also worth highlighting that substantia nigra free water levels estimated with a diffusion MRI bi-tensor model have recently been proposed as a novel biomarker in Parkinson's disease (Ofori *et al.*, 2015) – a selective pattern of progressive free water elevation that stands in stark contrast to the more widespread involvement found for other extra-pyramidal disorders (Planetta *et al.*, 2016). Combining QSM and free water levels—as surrogates for iron content and cellularity, respectively—in future studies may, therefore, offer added value in exploring nigral integrity.

Globus pallidus

In contrast to the substantia nigra, only a non-significant QSM increase was observed in the globus pallidus of Parkinson's disease patients. Notably, post-mortem reports of pallidal iron content are inconclusive; while some studies have shown an increase in Parkinson's disease (Chen *et al.*, 1993), others showed normal levels (Riederer *et al.*, 1989; Sofic *et al.*, 1991) or even reductions (Dexter *et al.*, 1991). Differences across experimental procedures and quantification techniques could explain the discrepancy (Hare *et al.*, 2012), though a key possibility might be inferred from one study (Griffiths *et al.*, 1999) that revealed iron content decreased in pars interna and increased in pars externa in Parkinson's disease. It is conceivable, therefore, these effects could cancel each other when studying the whole globus pallidus with regions of interest or by the effect of spatial smoothing (a necessary step in co-registration based analyses of the whole brain). There may also be a temporal dimension that could explain the discordant pallidal iron results in Parkinson's disease: QSM elevation has been reported in moderate—mean UPDRS-III=44.5±13.1—but not early disease stages—mean UPDRS-III=22.8±11.7 (Guan *et al.*, In Press, DOI: 10.1002/nbm.3489, available online 8 February 2016)—consistent with the present negative pallidal results in a Parkinson's disease cohort with a mean UPDRS-III of 16.3±8.0, therefore suggesting that pallidal iron loading may be a relative late disease feature.

Striatum

Another relevant negative in the present study was the lack of significant alterations in the normally iron-rich striatum. This negative is compatible with many post-mortem (Riederer *et al.*, 1989; Dexter *et al.*, 1991; Sofic *et al.*, 1991) and *in vivo* region of interest studies using the apparent proton transverse relaxation rate i.e. R_2* (Martin *et al.*, 2008; Du *et al.*, 2012; Barbosa *et al.*, 2015; He *et al.*, 2015; Murakami *et al.*, 2015), homodyne-filtered phase mapping (Han *et al.*, 2013; Kim and Lee, 2014) or QSM (Barbosa *et al.*, 2015; He *et al.*, 2015; Murakami *et al.*, 2015). This observation finds resonance with the view that dopamine responsiveness in Parkinson's disease relates to the preserved striatal targets of the degenerating nigrostriatal dopaminergic neurons, which could also lead to the prediction that Parkinson-plus diseases such as progressive supranuclear palsy and multiple system atrophy might show additional QSM changes in the corpus striatum (Dexter *et al.*, 1991; Han *et al.*, 2013).

Cerebellum

An interesting observation in the age-corrected region of interest analysis was a significant QSM reduction in the cerebellar dentate nucleus (Fig. 6). This structure has typically not been considered

in post-mortem Parkinson's disease analyses, but there is at least one precedent where a marked iron reduction was found in the dentate nucleus (Riederer *et al.*, 1989), though the observation was not discussed further. In health, the cerebellar dentate is one of the most iron-rich structures in the brain (Hallgren and Sourander, 1958) and therefore returns high QSM values (Acosta-Cabronero *et al.*, 2016). In the elderly, however, dentate susceptibility estimates become dispersed—in comparison to young adults—including a small minority of cases with very low values (Acosta-Cabronero *et al.*, 2016). It appears that low values become very prevalent in Parkinson's disease. The reduction in some individuals was extreme in the present study (Fig. 4 and 5); whether this might have phenotypic significance should be a topic for future research. The patient cohort in this study was predominantly akinetic-rigid Parkinson's disease (only three tremor-dominant cases), thus decreased QSM appears to be concordant with a recent study that has hinted at dentate QSM being associated with phenotypic differences in that tremor-predominant cases returned increased values, whereas there was a trend to reduced susceptibility in akinetic-rigid Parkinson's disease (He *et al.*, In Press, DOI: 10.1002/nbm.3554, available online 18 May 2016). One other study found no changes in the dentate in Parkinson's disease, although the acquisition was very brief and relatively low resolution therefore risking loss of sensitivity (Guan *et al.*, In Press, DOI: 10.1002/nbm.3489, available online 8 February 2016). There is growing interest in the role of the cerebellum in Parkinson's disease with the discovery of disynaptic pathways linking cerebellum to basal ganglia (Bostan *et al.*, 2013) and with numerous studies highlighting cerebellar hyperactivation during motor tasks or increased resting functional connectivity – reviewed elsewhere (Wu and Hallett, 2013). Physiological changes such as these may be secondary or compensatory but the present finding of apparent loss of iron content in the dentate points to local cerebellar alterations—a finding that should be investigated further histologically.

Cortex

An advantage of the present MRI approach over other established means of probing brain iron such as histochemical analysis, staining methods or transcranial sonography is that MRI can image the whole brain in a few minutes, thus making it an ideal tool to characterise the cortical pattern of iron deposition *in vivo*. The present whole-brain results (Fig. 2)—the first of their kind in Parkinson's disease—revealed a distribution of QSM abnormalities in the cortex that was in close agreement with the suspected landscape of Lewy inclusion pathology (Hughes *et al.*, 1992; Braak *et al.*, 2004) and glucose hypometabolism in autopsy-confirmed Lewy body disease (Minoshima *et al.*, 2001). In clinical stages, these predict concurrent involvement of limbic and paralimbic structures of the temporal lobe, prefrontal cortex and isocortical sensory-association areas with relative sparing of primary sensory areas—a distribution highly consistent with the QSM results in this study. Such

concordance between markers of pathology, iron accumulation and neuronal loss does not yet clarify whether iron is cause or consequence of Parkinson's disease degeneration, it cannot resolve either whether iron dysregulation occurs through uptake, storage or transport mechanisms, or whether excess iron is in free form or bound to macromolecules, but reinforces the notion that in Parkinson's disease there is a deleterious cocktail of Lewy inclusions and iron elevation across the isocortex. The causative theory that iron accumulation is an upstream event to Lewy pathology, however, could be entertained. It could be argued that although the distribution of cortical increase in QSM in the present study shows homology with the known distribution of glucose hypometabolism and Lewy pathology once this pathology has reached the neocortex, it does not follow that pathological burden causing neuronal dysfunction and iron accumulation are contemporaneous events. In fact, given that the current cohort generally had preserved cognition, it is possible that the cohort were not yet significantly affected by neocortical Lewy pathology—symptomatic Parkinson's disease is thought to begin with Braak stage 4 α-synuclein pathology (Braak *et al.*, 2003) in which the neocortex is yet to be affected. There is no way at present to directly investigate this *in vivo* because imaging techniques that visualise α-synuclein are not yet available. Though it would be intriguing to investigate, post-mortem, whether increases in neocortical iron concentration are detectable in Parkinson's disease brains without neocortical Lewy pathology (i.e. Braak stage<5). Nonetheless, even if iron imbalance was an indirect consequence of other primary causes, a mirroring distribution would still be highly relevant for the purpose of disease monitoring as it would mean iron mapping could act as proxy signature of cortical pathology.

Biomarker relevance

The QSM findings stand in stark contrast to the lack of significant findings using conventional MRI methods namely voxel-based morphometry, cortical thickness analysis, subcortical volumetry and tract-based DTI analysis. The negative findings with these methods were not unexpected; for instance, even in dementia with Lewy bodies, structural imaging to detect atrophy is largely unremarkable (Whitwell *et al.*, 2007) while previous tract-based DTI studies have also been negative (Worker *et al.*, 2014). Though notably, diffusion MRI using a bi-tensor model, as previously discussed, could offer a sensitive marker to study the substantia nigra (Ofori *et al.*, 2015), which is usually excluded from DTI analyses due to low diffusion anisotropy and other reliability concerns. The absence, however, of consistent findings with standard structural MRI/DTI methods highlights the potential of probing tissue iron across the whole brain with QSM as a useful biomarker in Parkinson's disease.

Note on QSM interpretations

A broad assumption in this study was that QSM alterations in Parkinson's disease reflect changes in iron content. Such interpretation, however, merits further discussion on the basis that the intrinsic magnetostatic properties of human brain tissue are not be driven by iron alone. Copper(II) and manganese compounds are magnetically reactive and could perturb the susceptibility measurement; although with concentrations 15 and 50 times lower, respectively, than iron in the substantia nigra (Krebs *et al.*, 2014), it is highly improbable they could have played a significant role in the present results. Furthermore, post-mortem studies have suggested that copper levels are slightly reduced in the substantia nigra in Parkinson's disease (Dexter *et al.*, 1991; Davies *et al.*, 2014), while manganese levels are largely unaltered (Dexter *et al.*, 1991). Abnormally high levels of zinc, in contrast, have been detected in several post-mortem Parkinson's disease brain regions. Zinc too, however, is scarce relative to iron content and does not have an unpaired electron configuration; consequently, the impact of zinc on QSM can also be discarded. Diamagnetic alkaline earth metals, calcium and magnesium, are more abundant in human brain tissue than the aforementioned transition metals, with regional concentrations in post-mortem tissue similar—often greater—than those for iron (Krebs *et al.*, 2014). Conceivably, the effect of diamagnetic mineralisation could reduce QSM sensitivity to iron-related effects. Signed QSM, however, although less sensitive overall than absolute QSM presumably due to its greater vulnerability to neighbouring contamination (Betts *et al.*, 2016), returned increased susceptibility—consistent with increased iron content—across all affected areas. The exception was the dentate nucleus meaning that, in addition to a loss of iron, micro-calcifications could explain our QSM observations, and should thus be considered as a plausible theory in future post-mortem studies.

Three post-mortem validation studies that, to date, have been carried out to investigate the relationship between QSM and tissue iron concentrations (Langkammer *et al.*, 2012; Zheng *et al.*, 2013; Sun *et al.*, 2015) should also be considered in interpreting the present study. The conclusion from these studies was that ferric iron, presumably stored in glial ferritin, is the dominant source of magnetic susceptibility in metal-laden deep brain nuclei. In the cerebral cortex, however, it has been shown that the myeloarchitecture can modulate local tissue susceptibility (Fukunaga *et al.*, 2010; Stüber *et al.*, 2014). It is therefore plausible that demyelination processes – yielding a net increase in paramagnetism – could drive QSM effects in areas of relatively low iron concentration, e.g. prefrontal cortex. Both studies, however, demonstrated that ferritin iron co-localised with intra-cortical myelin is the dominant source of local susceptibility – approximately two thirds of the overall contrast proportion in grey matter (Stüber *et al.*, 2014) – suggesting, therefore, only a massive myelin-driven susceptibility effect could perturb the measurement. In future, a recently

proposed multivariate model could be applied to disentangle iron/myelin contributions using multi-contrast information (Stüber *et al.*, 2014). All of the above, nonetheless, suggests the present *in vivo* results are most likely driven by changes in iron content, although QSM's inability to provide information about the exact cellular distribution or the valency of iron ions means the present results cannot discern whether QSM alterations in Parkinson's disease are primarily driven by excess free iron, greater ferritin numbers, greater iron loading within ferritin or neuromelanin, hemosiderin burden, or whether they represent neuronal or glial iron accumulation.

Finally, other technical limitations must be highlighted. The medulla oblongata has been postulated as one of the earliest sites of Lewy pathology in the Parkinson's disease cascade (Braak *et al.*, 2004), though here it did not return a significant QSM alteration. A plausible explanation for such absence could be that baseline iron levels are very low in medullar nuclei, thus small disease-related alterations—potentially large in relative terms—may lie undetected with current technology. In contrast, one should be careful of not over-interpreting whole-brain results in small anatomical structures. Prior to performing statistics, QSM data was spatially smoothed to account for possible errors in spatial normalisation, and although a smoothing-compensation strategy was applied, one should assume a degree of spatial uncertainty for the resulting clusters. This is particularly relevant to Braak stage 1-2 (Braak *et al.*, 2004) brainstem nuclei such as the motor nucleus of the vagus nerve, locus coeruleus or raphe nucleus that are probably too small to be reliably assessed using the present whole-brain methodology. On a final note, we must highlight that in the present study we were unable to establish QSM correlates of symptom severity measures, i.e. UPDRS-III and MMSE. Given the narrow spread of severity scores for the patient cohort under investigation (particularly for MMSE, see Supplementary Material) and a relatively low number of subjects for regression analyses, the risk of false-negative associations is very high. The relationship of QSM alterations to clinical parameters warrants a future investigation with greater statistical power and variance in the clinical data.

Conclusions

This study revealed a spatial distribution of QSM alterations in Parkinson's disease highly consistent with the landscapes of glucose hypometabolism and Lewy pathology that are known to emerge as the disease evolves. In contrast to QSM, no significant effects were observed with standard structural MRI and microstructural DTI measurements. These results, therefore, demonstrate the relevance of mapping the biochemical environment of the whole Parkinson's disease brain *in vivo*, and provide new insights into the behaviour of QSM as a disease biomarker.

MRI's safe and non-invasive nature means, in addition, that QSM might be suitable for longitudinal monitoring in clinical trials.

ACKNOWLEDGEMENTS

We are very grateful to all the participants who made this research possible. We also thank Mrs Urte Schneider, Ms Sabrina Rädler, Ms Deike Hartmann and our local radiographers—Mrs Kerstin Möhring and Mrs Ilona Wiedenhöft—for their invaluable help with subject recruitment, data collection and their dedicated efforts in scanning standardisation and quality assurance.

SUPPLEMENTARY MATERIAL

Supplementary material illustrating the regional QSM interplay with disease severity scores is available at *Brain* online.

REFERENCES

Acosta-Cabronero J, Betts MJ, Cardenas-Blanco A, Yang S, Nestor PJ. In Vivo MRI mapping of brain iron deposition across the adult lifespan. J Neurosci 2016; 36: 364-74.

Ayton S, Lei P. Nigral iron elevation is an invariable feature of Parkinson's disease and is a sufficient cause of neurodegeneration. Biomed Res Int 2014; 2014: 581256.

Barbosa JH, Santos AC, Tumas V, Liu M, Zheng W, Haacke EM*, et al.* Quantifying brain iron deposition in patients with Parkinson's disease using quantitative susceptibility mapping, R2 and R2*. Magn Reson Imaging 2015; 33: 559-65.

Betts MJ, Acosta-Cabronero J, Cardenas-Blanco A, Nestor PJ, Duezel E. High-resolution characterisation of the aging brain using simultaneous quantitative susceptibility mapping (QSM) and R2* measurements at 7 T. Neuroimage 2016; 138: 43-63.

Blazejewska AI, Schwarz ST, Pitiot A, Stephenson MC, Lowe J, Bajaj N*, et al.* Visualization of nigrosome 1 and its loss in PD: pathoanatomical correlation and in vivo 7 T MRI. Neurology 2013; 81: 534-40.

Bostan AC, Dum RP, Strick PL. Cerebellar networks with the cerebral cortex and basal ganglia. Trends Cogn Sci 2013; 17: 241-54.

Braak H, Del Tredici K, Rub U, de Vos RA, Jansen Steur EN, Braak E. Staging of brain pathology related to sporadic Parkinson's disease. Neurobiol Aging 2003; 24: 197-211.

Braak H, Ghebremedhin E, Rub U, Bratzke H, Del Tredici K. Stages in the development of Parkinson's disease-related pathology. Cell Tissue Res 2004; 318: 121-34.

Chen JC, Hardy PA, Kucharczyk W, Clauberg M, Joshi JG, Vourlas A*, et al.* MR of human postmortem brain tissue: correlative study between T2 and assays of iron and ferritin in Parkinson and Huntington disease. AJNR Am J Neuroradiol 1993; 14: 275-81.

Damier P, Hirsch EC, Agid Y, Graybiel AM. The substantia nigra of the human brain. II. Patterns of loss of dopamine-containing neurons in Parkinson's disease. Brain 1999; 122: 1437-48.

Davies KM, Bohic S, Carmona A, Ortega R, Cottam V, Hare DJ*, et al.* Copper pathology in vulnerable brain regions in Parkinson's disease. Neurobiol Aging 2014; 35: 858-66.

Dexter DT, Carayon A, Javoy-Agid F, Agid Y, Wells FR, Daniel SE*, et al.* Alterations in the levels of iron, ferritin and other trace metals in Parkinson's disease and other neurodegenerative diseases affecting the basal ganglia. Brain 1991; 114: 1953-75.

Du G, Lewis MM, Shaffer ML, Chen H, Yang QX, Mailman RB*, et al.* Serum cholesterol and nigrostriatal R2* values in Parkinson's disease. PLoS One 2012; 7: e35397.

Fearnley JM, Lees AJ. Ageing and Parkinson's disease: substantia nigra regional selectivity. Brain 1991; 114: 2283-301.

Folstein MF, Folstein SE, McHugh PR. "Mini-mental state". A practical method for grading the cognitive state of patients for the clinician. J Psychiatr Res 1975; 12: 189-98.

Fukunaga M, Li TQ, van Gelderen P, de Zwart JA, Shmueli K, Yao B*, et al.* Layer-specific variation of iron content in cerebral cortex as a source of MRI contrast. Proc Natl Acad Sci U S A 2010; 107: 3834-9.

Good PF, Olanow CW, Perl DP. Neuromelanin-containing neurons of the substantia nigra accumulate iron and aluminum in Parkinson's disease: a LAMMA study. Brain Res 1992; 593: 343-6.

Griffiths PD, Dobson BR, Jones GR, Clarke DT. Iron in the basal ganglia in Parkinson's disease. An in vitro study using extended X-ray absorption fine structure and cryo-electron microscopy. Brain 1999; 122: 667-73.

Griswold MA, Jakob PM, Heidemann RM, Nittka M, Jellus V, Wang J*, et al.* Generalized autocalibrating partially parallel acquisitions (GRAPPA). Magn Reson Med 2002; 47: 1202-10.

Groeger A, Berg D. Does structural neuroimaging reveal a disturbance of iron metabolism in Parkinson's disease? Implications from MRI and TCS studies. J Neural Transm 2012; 119: 1523-8.

Guan X, Xuan M, Gu Q, Huang P, Liu C, Wang N*, et al.* Regionally progressive accumulation of iron in Parkinson's disease as measured by quantitative susceptibility mapping. NMR Biomed In Press, DOI: 10.1002/nbm.3489, available online 8 February 2016.

Hallgren B, Sourander P. The effect of age on the non-haemin iron in the human brain. J Neurochem 1958; 3: 41-51.

Han YH, Lee JH, Kang BM, Mun CW, Baik SK, Shin YI*, et al.* Topographical differences of brain iron deposition between progressive supranuclear palsy and parkinsonian variant multiple system atrophy. J Neurol Sci 2013; 325: 29-35.

Hare DJ, Double KL. Iron and dopamine: a toxic couple. Brain In Press, DOI: 10.1093/brain/aww022, available online 8 March 2016.

Hare DJ, Gerlach M, Riederer P. Considerations for measuring iron in post-mortem tissue of Parkinson's disease patients. J Neural Transm 2012; 119: 1515-21.

He N, Huang P, Ling H, Langley J, Liu C, Ding B*, et al.* Dentate nucleus iron deposition is a potential biomarker for tremor-dominant Parkinson's disease. NMR Biomed In Press, DOI: 10.1002/nbm.3554, available online 18 May 2016.

He N, Ling H, Ding B, Huang J, Zhang Y, Zhang Z*, et al.* Region-specific disturbed iron distribution in early idiopathic Parkinson's disease measured by quantitative susceptibility mapping. Hum Brain Mapp 2015; 36: 4407-20.

Hirsch E, Graybiel AM, Agid YA. Melanized dopaminergic neurons are differentially susceptible to degeneration in Parkinson's disease. Nature 1988; 334: 345-8.

Hughes AJ, Daniel SE, Kilford L, Lees AJ. Accuracy of clinical diagnosis of idiopathic Parkinson's disease: a clinico-pathological study of 100 cases. J Neurol Neurosurg Psychiatry 1992; 55: 181-4.

Jack CR, Jr., Twomey CK, Zinsmeister AR, Sharbrough FW, Petersen RC, Cascino GD. Anterior temporal lobes and hippocampal formations: normative volumetric measurements from MR images in young adults. Radiology 1989; 172: 549-54.

Kim TH, Lee JH. Serum uric acid and nigral iron deposition in Parkinson's disease: a pilot study. PLoS One 2014; 9: e112512.

Klein A, Tourville J. 101 labeled brain images and a consistent human cortical labeling protocol. Front Neurosci 2012; 6: 171.

Krebs N, Langkammer C, Goessler W, Ropele S, Fazekas F, Yen K*, et al.* Assessment of trace elements in human brain using inductively coupled plasma mass spectrometry. J Trace Elem Med Biol 2014; 28: 1-7.

Kwon DH, Kim JM, Oh SH, Jeong HJ, Park SY, Oh ES*, et al.* Seven-Tesla magnetic resonance images of the substantia nigra in Parkinson disease. Ann Neurol 2012; 71: 267-77.

Langkammer C, Schweser F, Krebs N, Deistung A, Goessler W, Scheurer E*, et al.* Quantitative susceptibility mapping (QSM) as a means to measure brain iron? A post mortem validation study. Neuroimage 2012; 62: 1593-9.

Lehericy S, Bardinet E, Poupon C, Vidailhet M, Francois C. 7 Tesla magnetic resonance imaging: a closer look at substantia nigra anatomy in Parkinson's disease. Mov Disord 2014; 29: 1574-81.

Li W, Jiang H, Song N, Xie J. Oxidative stress partially contributes to iron-induced alpha-synuclein aggregation in SK-N-SH cells. Neurotox Res 2011; 19: 435-42.

Liu T, Wisnieff C, Lou M, Chen W, Spincemaille P, Wang Y. Nonlinear formulation of the magnetic field to source relationship for robust quantitative susceptibility mapping. Magn Reson Med 2013; 69: 467-76.

Martin WR, Wieler M, Gee M. Midbrain iron content in early Parkinson disease: a potential biomarker of disease status. Neurology 2008; 70: 1411-7.

Minoshima S, Foster NL, Sima AA, Frey KA, Albin RL, Kuhl DE. Alzheimer's disease versus dementia with Lewy bodies: cerebral metabolic distinction with autopsy confirmation. Ann Neurol 2001; 50: 358-65.

Murakami Y, Kakeda S, Watanabe K, Ueda I, Ogasawara A, Moriya J*, et al.* Usefulness of quantitative susceptibility mapping for the diagnosis of Parkinson disease. AJNR Am J Neuroradiol 2015; 36: 1102-8.

Oakley AE, Collingwood JF, Dobson J, Love G, Perrott HR, Edwardson JA*, et al.* Individual dopaminergic neurons show raised iron levels in Parkinson disease. Neurology 2007; 68: 1820-5.

Ofori E, Pasternak O, Planetta PJ, Li H, Burciu RG, Snyder AF*, et al.* Longitudinal changes in free-water within the substantia nigra of Parkinson's disease. Brain 2015; 138: 2322-31.

Ostrerova-Golts N, Petrucelli L, Hardy J, Lee JM, Farer M, Wolozin B. The A53T alpha-synuclein mutation increases iron-dependent aggregation and toxicity. J Neurosci 2000; 20: 6048-54.

Patenaude B, Smith SM, Kennedy DN, Jenkinson M. A Bayesian model of shape and appearance for subcortical brain segmentation. Neuroimage 2011; 56: 907-22.

Pengas G, Pereira JM, Williams GB, Nestor PJ. Comparative reliability of total intracranial volume estimation methods and the influence of atrophy in a longitudinal semantic dementia cohort. J Neuroimaging 2009; 19: 37-46.

Planetta PJ, Ofori E, Pasternak O, Burciu RG, Shukla P, DeSimone JC*, et al.* Free-water imaging in Parkinson's disease and atypical parkinsonism. Brain 2016; 139: 495-508.

Popescu BF, George MJ, Bergmann U, Garachtchenko AV, Kelly ME, McCrea RP*, et al.* Mapping metals in Parkinson's and normal brain using rapid-scanning x-ray fluorescence. Phys Med Biol 2009; 54: 651-63.

Riederer P, Sofic E, Rausch WD, Schmidt B, Reynolds GP, Jellinger K*, et al.* Transition metals, ferritin, glutathione, and ascorbic acid in parkinsonian brains. J Neurochem 1989; 52: 515-20.

Schofield MA, Zhu Y. Fast phase unwrapping algorithm for interferometric applications. Opt Lett 2003; 28: 1194-6.

Schweser F, Deistung A, Lehr BW, Reichenbach JR. Quantitative imaging of intrinsic magnetic tissue properties using MRI signal phase: an approach to in vivo brain iron metabolism? Neuroimage 2011; 54: 2789-807.

Sian-Huelsmann J, Mandel S, Youdim MB, Riederer P. The relevance of iron in the pathogenesis of Parkinson's disease. J Neurochem 2011; 118: 939-57.

Smith SM, Jenkinson M, Johansen-Berg H, Rueckert D, Nichols TE, Mackay CE*, et al.* Tract-based spatial statistics: voxelwise analysis of multi-subject diffusion data. Neuroimage 2006; 31: 1487-505.

Smith SM, Nichols TE. Threshold-free cluster enhancement: addressing problems of smoothing, threshold dependence and localisation in cluster inference. Neuroimage 2009; 44: 83-98.

Sofic E, Paulus W, Jellinger K, Riederer P, Youdim MB. Selective increase of iron in substantia nigra zona compacta of parkinsonian brains. J Neurochem 1991; 56: 978-82.

Stüber C, Morawski M, Schaefer A, Labadie C, Waehnert M, Leuze C*, et al.* Myelin and iron concentration in the human brain: a quantitative study of MRI contrast. Neuroimage 2014; 93: 95-106.

Sun H, Walsh AJ, Lebel RM, Blevins G, Catz I, Lu JQ*, et al.* Validation of quantitative susceptibility mapping with Perls' iron staining for subcortical gray matter. Neuroimage 2015; 105: 486-92.

Walsh DO, Gmitro AF, Marcellin MW. Adaptive reconstruction of phased array MR imagery. Magn Reson Med 2000; 43: 682-90.

Ward RJ, Zucca FA, Duyn JH, Crichton RR, Zecca L. The role of iron in brain ageing and neurodegenerative disorders. Lancet Neurol 2014; 13: 1045-60.

Whitwell JL, Weigand SD, Shiung MM, Boeve BF, Ferman TJ, Smith GE*, et al.* Focal atrophy in dementia with Lewy bodies on MRI: a distinct pattern from Alzheimer's disease. Brain 2007; 130: 708-19.

Winkler AM, Ridgway GR, Webster MA, Smith SM, Nichols TE. Permutation inference for the general linear model. Neuroimage 2014; 92: 381-97.

Worker A, Blain C, Jarosz J, Chaudhuri KR, Barker GJ, Williams SC*, et al.* Diffusion tensor imaging of Parkinson's disease, multiple system atrophy and progressive supranuclear palsy: a tract-based spatial statistics study. PLoS One 2014; 9: e112638.

Wu T, Hallett M. The cerebellum in Parkinson's disease. Brain 2013; 136: 696-709.

Zheng W, Nichol H, Liu S, Cheng YC, Haacke EM. Measuring iron in the brain using quantitative susceptibility mapping and X-ray fluorescence imaging. Neuroimage 2013; 78: 68-74.

Supplementary Material

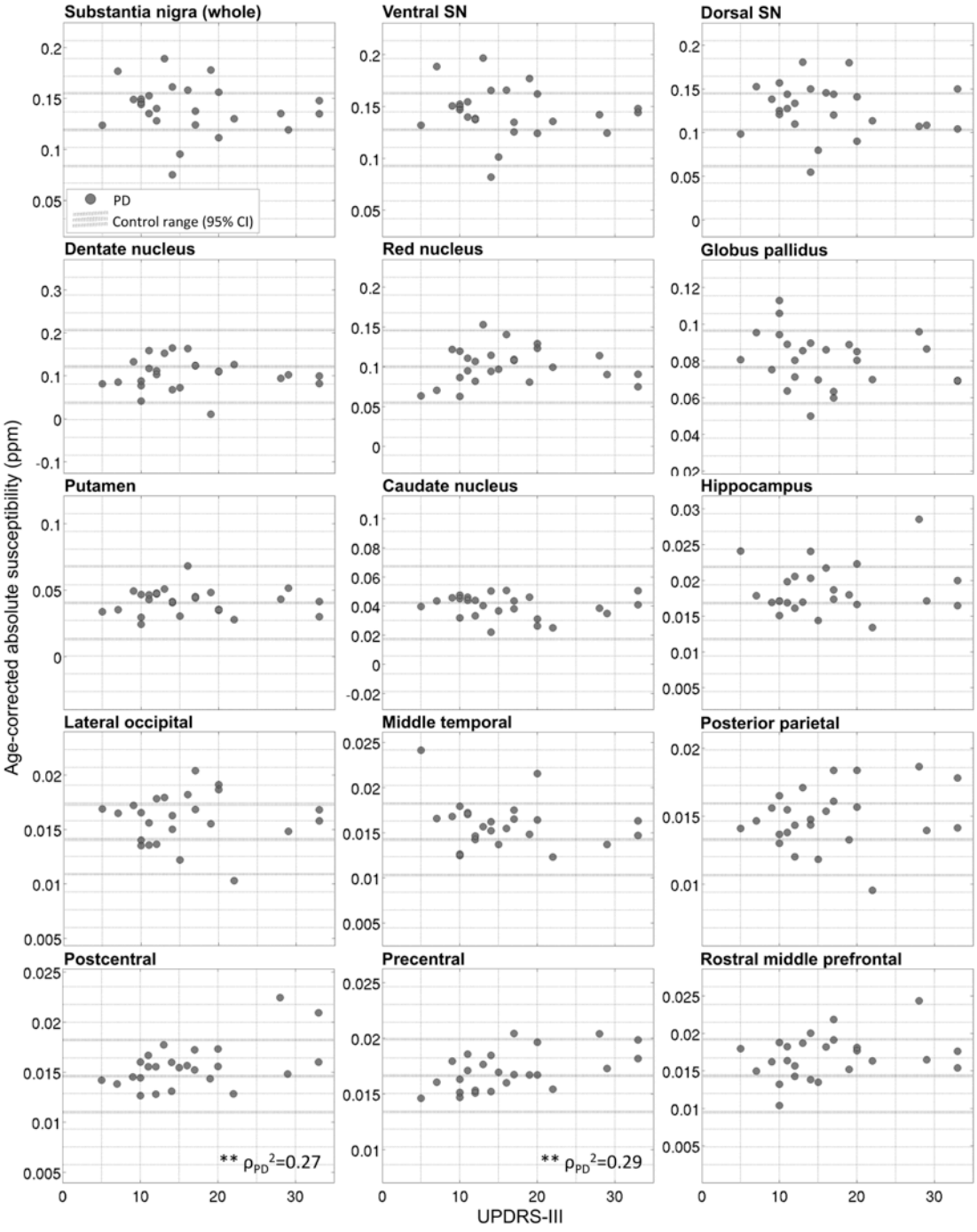

Supplementary Figure 1. Regional QSM versus UPDRS-III. Age-adjusted median QSM values in Parkinson's disease plotted as a function of motor status. Stars signify the strength of the correlation in the patient group (** P<0.01).

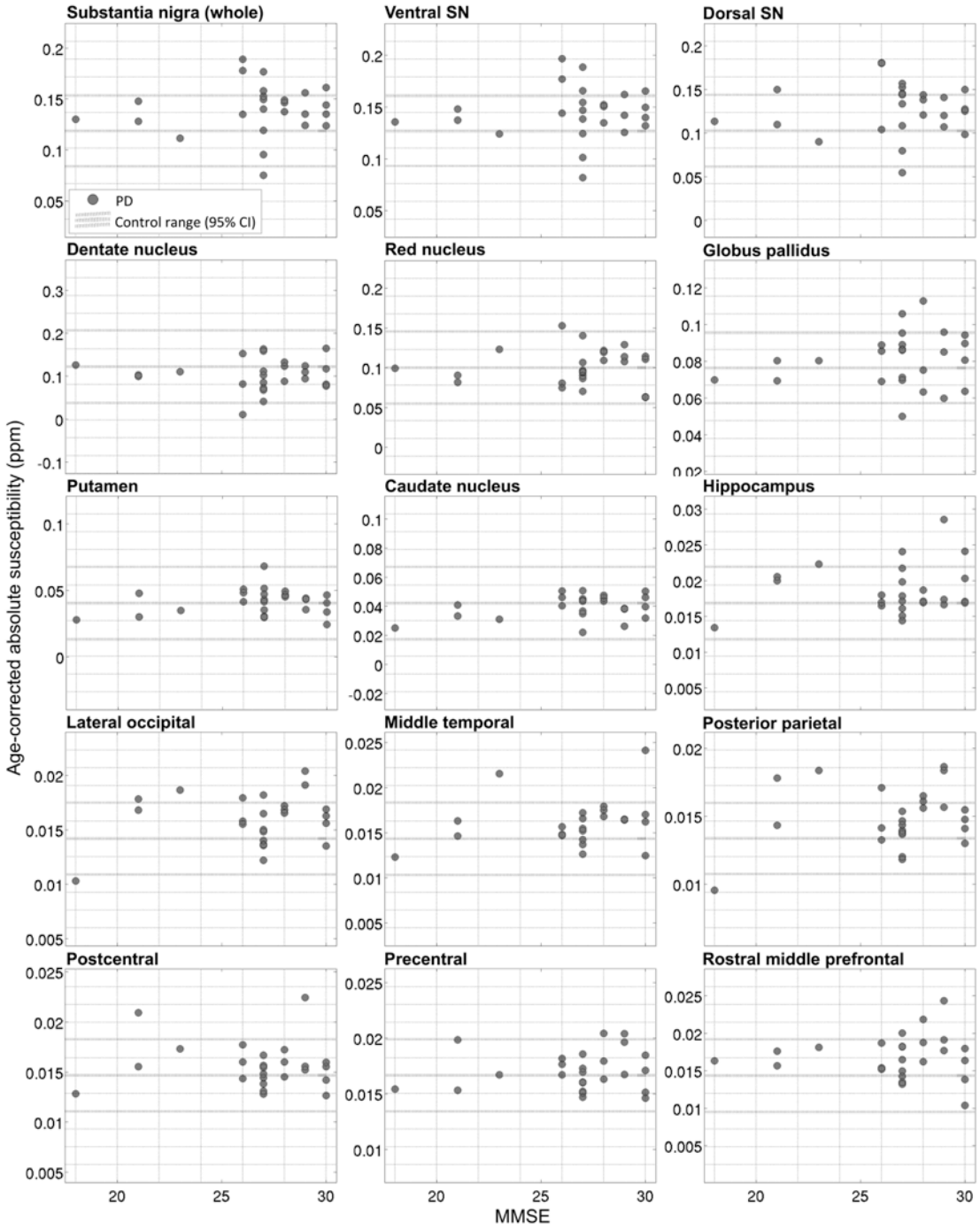

Supplementary Figure 2. Regional QSM versus MMSE. Age-adjusted median QSM values in Parkinson's disease plotted as a function of cognitive status.